### Title

Turning water into a protonic diode and solar cell via doping and dye sensitization




### Journal

Joule, 5(9)

### ISSN

2542-4351



### Authors

Schulte, Leanna

White, William

Renna, Lawrence A

et al.



### Publication Date

2021-09-01

### DOI

10.1016/j.joule.2021.06.016

CellPress

Joule

Article

# Turning water into a protonic diode and solar cell via doping and dye sensitization

Leanna Schulte,[1] William White,[1] Lawrence A. Renna,[1] and Shane Ardo[1,2,3,4,*]

## SUMMARY

**The key advance that led to the digital revolution was the invention of the solid-state diode, due to its ability to effectively rectify electronic current. Analogous, water-based diodes were invented around the same time, yet their ability to rectify protonic current paled in comparison. A suitable platform to fabricate water-based diodes is the bipolar ion-exchange membrane, which serves as a scaffold for dopants that ionize when infiltrated with protonically semiconducting water. Herein, by fashioning bipolar membranes into membrane-electrode assemblies and characterizing them like fuel cells, we report high-quality protonic diodes that, when sensitized to visible light using photoacids, exhibit "reverse" photovoltaic action. These demonstrations will spur innovations in the fields of iontronics, neuromorphic computing, and brain-machine interfaces, among others.**

## INTRODUCTION

Rectifiers, transistors, switches, and photodetectors have led to many of society's recent technological advances. The core circuit element found in each of these constructs is the electronic diode.[1–3] Its effectiveness stems from its ability to rectify current well, a function that was engineered into diodes based on strong foundational knowledge. Diode function has been adequately modeled using analytical equations to predict relationships between current and voltage,[4,5] responses to direct, transient, and alternating currents,[5] and solar cell function when coupled to photon absorption.[6,7] Although purely electronic processes are at the core of the aforementioned diodes, the equations and relationships used to describe their function have also been applied to electrochemical systems where both electronic and ionic mobile charged species are coupled through redox reactions.[8,9] This has led to great advances in ion-gated switches,[10,11] chemical sensors,[12] and constructs for photoelectrochemical energy conversion.[13,14] Although electronic and mixed ionic-electronic diodes and resulting devices are now commonplace, reports of purely ionic diodes are far less common,[15,16] and the subset of protonic diodes—which are direct analogs of electronic semiconductors—are nearly absent from the literature.[17–21]

Fabrication of effective diodes requires controlled doping of the semiconductors that form them, using design principles that are agnostic to whether mobile charged species are electronic (electrons/holes) or protonic (protons/hydroxides).[22] Doping is achieved by introducting neutrally charged species into the semiconductor, whose energetics result in substantial dissociation into two oppositely charged species: one that is mobile and the other that is fixed. By contacting two semiconducting phases that contain oppositely charged majority mobile species, recombination occurs at the interface, leaving behind oppositely charged phases that present a unidirectional electrostatic space-charge region. Application of a potential bias to

### Context & scale

Protons and electrons are both fundamental particles whose dynamics of transport and chemical reactivity are driven by electromagnetic forces. Although this fact has resulted in a multitude of applications for solid-state materials that conduct electrons, significantly fewer applications exist for materials that conduct protons. Protons are ubiquitous in protic solvents, where the most well-known and abundant one is water. Therefore, by using water as a proton-transfer medium, analogs to electronic devices can be developed. These devices may prove useful in applications where water is inherently present, such as biological contexts and most large-scale electrochemical energy-conversion devices. We believe that the development of protonic devices will spur innovations in other more forward-looking fields, such as iontronics, neuromorphic computing, and brain-machine interfaces.

inject mobile charged species into and out of the space-charge region results in asymmetric charge flow, as current rectification. Since protonically semiconducting water is a liquid, dopants cannot simply be introduced as soluble Brønsted-Lowry acids and bases, e.g., HCl, KOH, because all species would be mobile and the resulting electric potential drops would be small, spatially random, and not result in current rectification. This can be remedied by infiltrating water into a scaffold used to fix dopants in place, as demonstrated by Bockris and coworkers over half a century ago,[16] by contacting two polymer scaffolds, one with fixed proton-donor groups and the other with fixed hydroxide-donor groups, into what is termed as a bipolar membrane.

Herein, we report detailed photoelectrochemical characterization of purely protonic pn-junction diodes consisting of bipolar-membrane-electrode assemblies that are also sensitized to visible light using covalently bonded photoacids.[23] Protonic diode performance was assessed using a potentiostat to drive two reversible and energy-efficient redox reactions to convert electronic power into protonic power. Solar cell function was measured when photogenerated protonic power was transduced into electronic power via the same intervening redox reactions.

## RESULTS AND DISCUSSION

### Bipolar-membrane-electrode assembly fabrication

Bipolar membranes were formed by drop casting an n-type Sustainion XA-9 ionomer (5% in ethanol) directly onto a p-type perfluorosulfonic acid cation-exchange membrane, with or without covalently bound photoacid dyes, and then heating at 80°C for 1 h. These bipolar membranes were then fabricated into membrane-electrode assemblies by applying reversible-hydrogen-electrode inks with an airbrush gun to sufficient coverage, such that current densities were not limited by mass transfer of $H_2$ (Figure S1) or charge transport in an ion-exchange material (Figure S2). Subsequently, the membrane-electrode assemblies were dialyzed in ultrapure water for >24 h to help remove ions other than $OH^-$ and $H^+$ (Figure S3). Electrochemical measurements were conducted using carbon-cloth current collectors and a visible-light-transmissive acrylic cell fed with 100% relative humidity forming gas (5/95 mol % $H_2$/$N_2$) to facilitate reversible $H_2$ redox chemistry at the electrodes (Reaction S1), with details in the supplemental information and supplemental experimental procedures. Figure 1 shows the bipolar-membrane-electrode assembly and the varied physical parameters and chemical processes proposed to occur under applied potential bias.

### Water-based protonic diode behavior

Current density ($J$) versus potential ($E$) data for a representative bipolar-membrane-electrode assembly are shown in Figure 2A, and are reasonably modeled by the following Butler-Volmer electrocatalyst equation:

$$J = J_o\left(e^{\frac{\alpha_a q(E-E_{eq,a})}{k_B T}} - e^{\frac{-\alpha_c q(E-E_{eq,c})}{k_B T}}\right) \quad \text{(Equation 1)}$$

where $J$ is the current density flowing through the system (A/cm$^2$), $J_o$ is the exchange current density (A/cm$^2$), $\alpha_i$ is the fraction of the applied potential that influences current in the anodic/cathodic (a/c) direction, $q$ is the elementary charge ($1.602 \times 10^{-19}$ C), $E$ is the applied DC potential bias (V), $E_{eq,i}$ is the potential of the system at equilibrium (V) with $E_{eq,a} = E_{eq,c}$, $k_B$ is the Boltzmann constant ($1.381 \times 10^{-23}$ J K$^{-1}$), and $T$ is the temperature (298.15 K). When $\alpha_c = 0$, Equation 1 is the Shockley diode equation, where $J_o$ represents the reverse saturation current density due to thermal generation of mobile charged species, $\alpha_a = \frac{1}{n_d}$ ($n_d$ is the diode quality factor), and $E_{eq,a} = E_{eq,c} = E_{oc}$ ($E_{oc}$ is the open-circuit potential). For both electrocatalysts and

[1]Department of Chemistry, University of California Irvine, Irvine, CA 92697, USA

[2]Department of Chemical & Biomolecular Engineering, University of California Irvine, Irvine, CA 92697, USA

[3]Department of Materials Science & Engineering, University of California Irvine, Irvine, CA 92697, USA

[4]Lead contact

*Correspondence: ardo@uci.edu

https://doi.org/10.1016/j.joule.2021.06.016

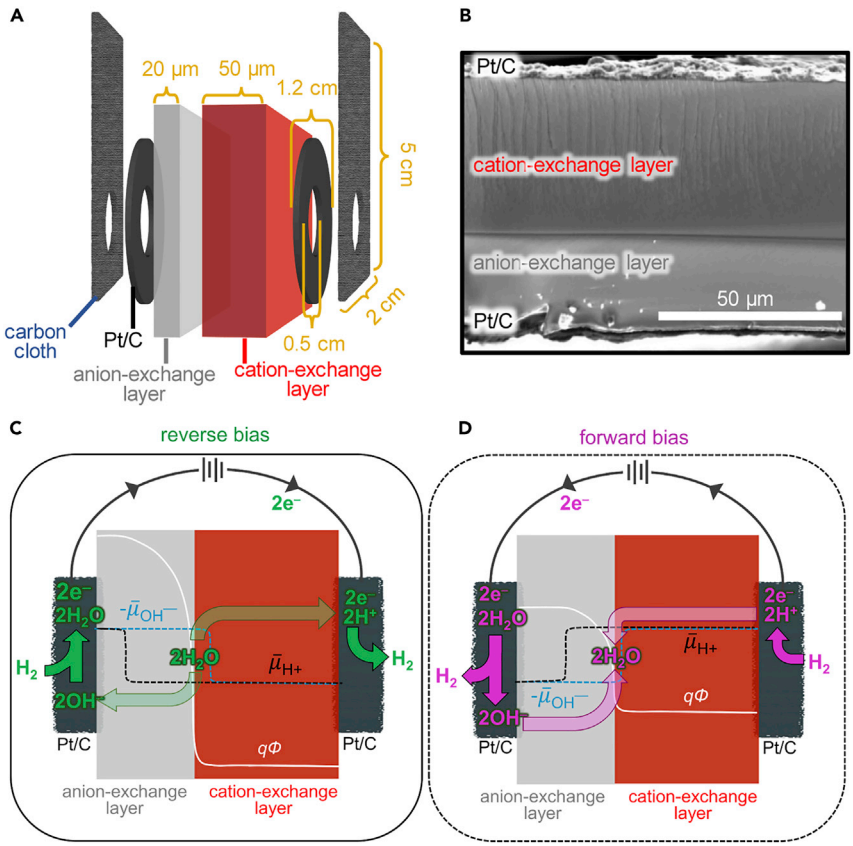


**Figure 1. Structure, physical parameters, and chemical processes of bipolar-membrane-electrode-assembly protonic diodes**

(A) Schematic of the membrane-electrode-assembly architecture.

(B) Scanning electron micrograph of a bipolar membrane with reversible-hydrogen gas-diffusion electrode catalyst layers and 50 μm scale bar.

(C and D) Schematics, analogous to band diagrams in solid-state physics, showing various physical parameters and chemical processes present during electrochemical measurement of a membrane-electrode-assembly protonic diode under reverse-bias and forward-bias conditions, where $\bar{\mu}_R$ stands for the electrochemical potential of R = $H^+$ or $OH^-$, and $\Phi$ is the electric potential felt by positively charged $H^+$. Because $H^+$ is the particle in our materials systems, these schematics are proton-centric, and therefore, depict distributions that, based on charge, are opposite of what would be depicted for analogous electronic diodes.

diodes, application of a potential bias modulates the electrochemical potentials of electrons and holes. Notwithstanding, the underlying physical processes that result in electrocatalytic behavior versus diode behavior are drastically different. For ideal metallic electrocatalysts, the interfacial electric potential distribution is altered, thereby influencing current via changes in activation free energy, and thus rate constants, of elementary reaction steps. For ideal pn-junction diodes, species concentrations, and thus species activities, in the space-charge depletion region are altered, thereby influencing current via mass action.

Although our bipolar-membrane-electrode assemblies are designed to function as ideal diodes with $\alpha_c = 0$, this is not observed experimentally. Instead, cathodic currents under reverse bias increase gradually in a rather exponential fashion, an effect previously ascribed to electric-field-enhanced (EFE) heterolytic water dissociation (WD).[24–29] Because the Poisson equation interconverts electric fields and electric

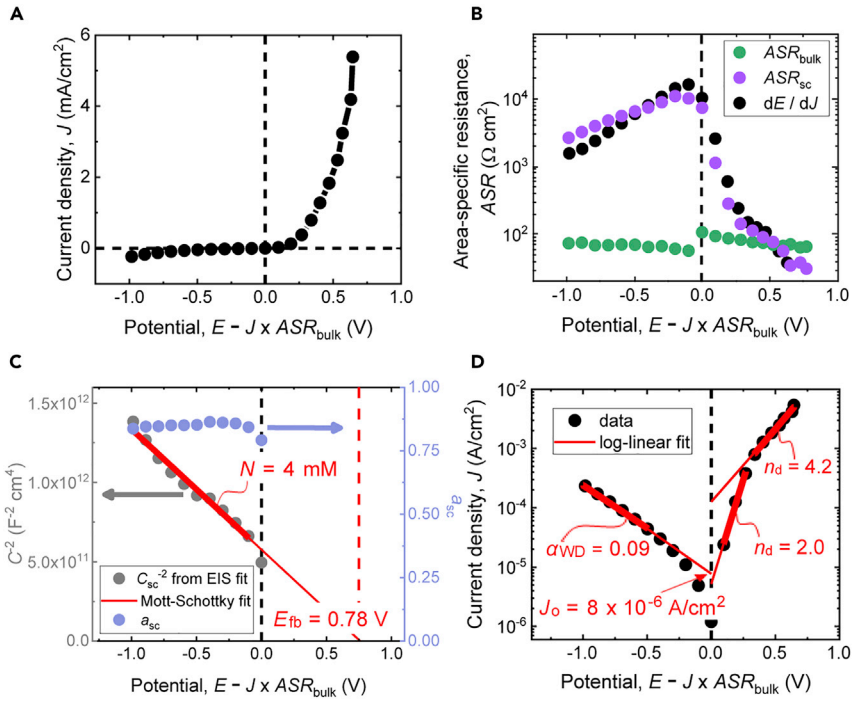


**Figure 2. Electrochemical data and analyses of one representative protonic diode**

(A) Current density ($J$) versus potential ($E$) data for net water dissociation under reverse bias, as depicted in Figure 1C, and net water formation under forward bias, as depicted in Figure 1D.

(B and C) (B) Area-specific resistances for protonic transport in the bulk ($ASR_{bulk}$) and across the space-charge depletion region ($ASR_{sc}$), and $^{dE}/_{dJ}$ obtained from the data in (A), and (C) capacitances ($C_{sc}$) and ideality factors ($a_{sc}$) of the space-charge depletion region extracted from best-fits of electrochemical impedance spectroscopy data to a nonideal Randles equivalent circuit model. Resistances are reported on a semilogarithmic plot, whereas capacitances are reported as a Mott-Schottky plot that includes a best-fit to the Mott-Schottky equation (Equation 2), with fitted region (bold line) and extrapolated region (thin line) shown, and extracted values indicated for the fixed-charge density in the space-charge depletion region ($N$) and extrapolation of the best-fit line to obtain the flatband potential ($E_{fb}$), as indicated by the red vertical dashed line. Electrochemical impedance spectroscopy data over the full range of applied potential biases are shown in Figure S4.

(D) Semilogarithmic plot of the data in (A) and best-fit to linearized versions of Equation 1, with fitted region (bold line) and extrapolated region (thin line) shown, and extracted values indicated for the diode quality factors ($n_d$), the fraction of the applied potential that influences the current for net water dissociation ($\alpha_{WD}$), and extrapolation of the reverse-bias best-fit line to obtain the exchange current density ($J_o$).

See also Figures S1–S6; Table S1.

potentials, the physical description and mathematical representation of this effect are identical to those used to derive the Butler-Volmer electrocatalyst equation.[9] As such, modification of the Shockley diode equation so that $J_o$ is exponentially dependent on $E$ results in Equation 1 with $E_{eq,c} = E_{fb}$ ($E_{fb}$ is the flatband potential, meaning the potential when the electric potential difference across the space-charge region equals zero), $E_{eq,a} = \left(\frac{\alpha_{WD} n_d}{\alpha_{WD} n_d - 1}\right) E_{fb}$, $\alpha_c = \alpha_{WD}$, and $\alpha_a = \frac{1}{n_d} - \alpha_{WD}$, meaning $n_d = \frac{1}{\alpha_a + \alpha_c}$ (derived in the supplemental information). $E_{fb}$ can be determined using Mott-Schottky analysis of area-specific-resistance-potential ($ASR_{sc}$–$E$) data (Figure 2B) and capacitance-potential ($C_{sc}^{-2}$–$E$) data (Figure 2C) for the space-charge (sc) region, obtained by fitting frequency-dependent electrochemical impedance spectroscopy data to a Randles equivalent-circuit model with nonideal

capacitor behavior represented by a constant-phase element, with details in the supplemental information and Table S1 and Figure S5.

Semilogarithmic plots of *ASR*–*E* data (Figure 2B) support that $ASR_{bulk}$ is near constant, a behavior that is expected for resistive contributions due to bulk transport of electrons and/or ions, and $ASR_{sc}$ decreases exponentially as the potential is varied from $E_{oc}$, a behavior that is consistent with a decrease in the resistance for charge transfer across the pn-junction space-charge depletion region due to an increase in the concentration of $H^+$ and $OH^-$. Behavior under anodic polarization is consistent with quasi-electrochemical-potential splitting that exists for forward-biased semiconductors,[30,31] whereas behavior under cathodic polarization is consistent with EFE-WD[24–29] due to increased electric fields present under reverse-bias conditions. Alternative explanations for these data were considered, including drift-dominated minority-carrier collection in the pn-junction space-charge region and bulk space-charge-limited conduction, but each was determined to be unlikely based on the linearity of the data in the Mott-Schottky plot (Figure 2C) and standard alternative analyses, with details in the supplemental information and Figure S5.

In order to determine $E_{fb}$, the linear reverse-bias region of $C_{sc}^{-2}$–*E* data were fitted and analyzed using the Mott-Schottky equation:

$$\frac{1}{C_{sc}^{\ 2}} = \frac{-2}{q\varepsilon_r\varepsilon_o N}\left(E - \left(E_{fb} - \frac{k_B T}{q}\right)\right) \qquad \text{(Equation 2)}$$

where $\varepsilon_r$ is the relative permittivity of water in the space-charge region and assumed to be that of hydrated Nafion (18),[32] $\varepsilon_o$ is the permittivity of vacuum ($8.854 \times 10^{-12}$ F $m^{-1}$), and *N* is the fixed-charge density in the space-charge region ($m^{-3}$). The best-fit lines for three protonic diodes resulted in $E_{fb} = 0.71 \pm 0.08$ V (= $\Phi_{bi}$, the built-in electric-potential difference) and $N = 3 \pm 2$ mM (Figure S5). This value of *N* is consistent with values reported for the anion-exchange material ($N_{AEM} \approx 10$ mM = $6 \times 10^{18}$ $cm^{-3}$)[33] and measured resistances for the individual anion-exchange layer (Figure S2), and is not consistent with measured or reported values for the cation-exchange material ($N_{CEM} \approx 1$ M = $6 \times 10^{20}$ $cm^{-3}$).[34] Moreover, assuming $N = N_{AEM}$ and that all ~1 M dopants in the cation-exchange layer are ionized, such that $N_{CEM} = 1$ M, $E_{fb}$ is within error of the expected value of 0.68 V ( = $k_B T \ln\left(\frac{N_{CEM}N_{AEM}}{K_w}\right)$,[5,31] where $K_w$ ($M^2$) has the value of the autoprotolysis equilibrium constant for bulk water (= $10^{-14}$)).

Semilogarithmic plots of *J*-*E* data (Figure 2D) are common when examining diode behavior in semiconductor physics[5,7] and electrocatalytic behavior in electrochemistry[9] to deduce accurate values for critical parameters, $n_d$ and $\alpha_{WD}$, and to analyze exponential behavior. After verifying that the exponential terms in Equation 1 will result in linear behavior on either side of $E_{oc}$ (derived in the supplemental information), we conclude that under forward bias, two distinct exponential regions exist with different values of $n_d$, a behavior that is consistent with interface-trap-state filling in standard diode models[7] and/or space-charge-limited conduction (Figure S5)[35,36] likely due to transport across the anion-exchange layer since $N_{AEM} < N_{CEM}$. In protonic diodes, trap states can consist of proton-donating and/or proton-accepting species whose $pK_a$ values lie in the range ($pK_a(H^+(aq))$, $pK_a(H_2O(aq))$) = (0, 14), such as impurity buffers like carbonate species. Best-fit lines for three protonic diodes resulted in $\alpha_{WD} = 0.09 \pm 0.01$, $n_{d,1} = 2.5 \pm 0.5$, and $J_o = 4 (\pm 4) \times 10^{-6}$ A/$cm^2$ (Figure S5). Values for $n_{d,1}$ are within error of those possible based on ideal diode performance, i.e., in the range [1, 2], with values for individual bipolar-membrane-electrode assemblies slightly exceeding this range, likely due to

nonideal capacitances observed for the space-charge region ($a_{sc}$ = 0.85 ± 0.02, where $a_{sc}$ = 1 is ideal). Diode current take-off under forward bias was more than four times as steep as EFE-WD current take-off under reverse bias.

Values for $J_o$ provide quantitative information about the rates of generation and recombination of $H^+$ and $OH^-$ in protonic diodes over a specified distance. Extrapolation of $J_o$ values measured at $E_{oc}$, where $\Phi_{bi}$ = 0.71 ± 0.08 V (= $E_{fb}$) and EFE-WD is operative, to $E_{fb}$, where $\Phi_{bi}$ = 0 and EFE-WD is not likely operative, results in $J_o'$ = 3 (± 2) × $10^{-7}$ A/$cm^2$ (mass flux, $N_o'$ = 3 [± 2] × $10^{-12}$ mol $cm^{-2}$ $s^{-1}$). Division of this intrinsic value of $N_o'$ by the autoprotolysis rate constant of bulk water, $k_0$ = 1.1 × $10^{-6}$ mol $cm^{-3}$ $s^{-1}$,[17] results in a value of 30 (± 20) nm. This is the predicted width over which quasi-electrochemical potentials for $H^+$ and $OH^-$ are split ($w_{q\text{-}ECP}$), meaning not at electrochemical equilibrium,[30,31] assuming that the properties of water in the bipolar membrane scaffold are the same as in bulk water. The similarity of $w_{q\text{-}ECP}$ (= 30 ± 20 nm) at $E_{oc}$ and the width of the space-charge depletion region ($w_{sc}$ = 23 ± 9 nm) predicted from Mott-Schottky data at $E_{oc}$ (Figure S5) suggests that minority-carrier drift lengths are on the order of $w_{sc}$, and that minority-carrier diffusion lengths are less than $w_{sc}$. These hypotheses are supported by results from numerical simulations, with details in the supplemental information and Figure S6, which provide credence that water in bipolar-membrane-electrode assemblies likely behaves similarly to bulk water.

## Light-to-protonic power conversion

One application for an ionic diode is as a photoelectrochemical solar cell, where absorption of light results in no net redox chemistry. Toward this, in our group's previous work we reported a salt-water-infiltrated photoacid-dye-sensitized cation-exchange membrane,[37,38] and later a bipolar membrane,[31,38] where the presence of salt species complicated analyses.[39] Herein, our highly engineered bipolar-membrane-electrode-assembly protonic diodes, uniquely fed with 100% relative humidity forming gas to facilitate reversible $H_2$ redox chemistry at the electrodes, were modified to serve as solar cells via covalent modification of poly(perfluorosulfonyl fluoride) Nafion precursor membranes with bondable photoacid dyes, 8-hydroxypyrene-1,3,6-trisulfonyl-ethylenediammonium chloride (Figure 3A).[37,40] Photovoltaic action from these materials is unequivocal (Figures 3B, S7, and S8), where both an open-circuit photovoltage, $V_{oc}$, and a short-circuit photocurrent density, $J_{sc}$, are apparent. Illumination results in a shift of *J–E* data, unexpectedly, into the 2nd quadrant and an increase in $ASR_{bulk}$ (Figure S9), observations consistent with a decrease in steady-state activity of $H^+$ and/or $OH^-$ and "reverse" photovoltaic action. Four protonic diodes, each sensitized with ~10 mM photoacid, yielded $V_{oc}$ = −33 (± 9) mV, $J_{sc}$ = 2 (± 1) × $10^{-6}$ A/$cm^2$ (< $J_o$), internal quantum yield at $J_{sc}$ (IQY) = −7 (± 5) × $10^{-3}$ %, and a simulated sunlight-to-electrical power conversion efficiency ($\eta_{solar}$) = −7 (± 6) × $10^{-6}$ % under 405 nm illumination at 1.7 Suns equivalent excitation (Figure S7), a simulated solar irradiance value that was calculated using a method we reported previously.[31,37,41] Notably, given the near-ideal values for $a_{sc}$, $n_d$, and $J_o'$, the small values for $\eta_{solar}$ are not a consequence of poor protonic diode performance. Instead, performance is limited by the "reverse" photovoltaic process, with a fill factor that is <0.25 by definition, and the fact that our photoacids photogenerate almost exclusively cationic $H^+$, yet not anionic $OH^-$,[42] which is unlike in traditional solar cells where cationic holes and anionic electrons are photogenerated simultaneously.

Although "reverse" photovoltaic action is reminiscent of that which occurs in thermoradiative cells, where photons are net emitted from a hotter material to colder surroundings,[43,44] this is not the mechanism that we propose herein. This is because $V_{oc}$ and $J_{sc}$ values were transient over >10 min of continuous illumination (Figures 3C, 3D, S7, and

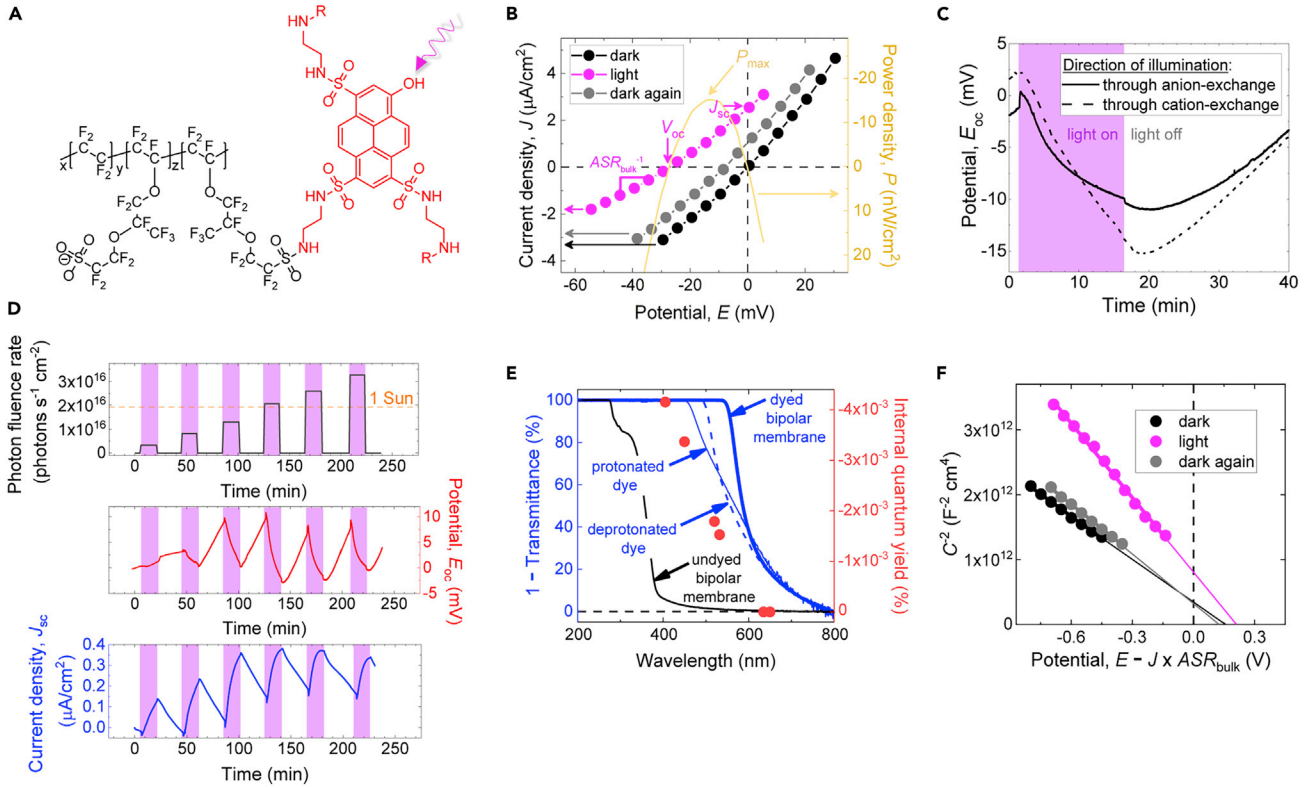


**Figure 3. Photoelectrochemical data and analyses of representative protonic solar cells**

(A) Chemical structure of pyrene-based photoacid dyes covalently bound to fixed-charge groups in the perfluorosulfonic acid cation-exchange membrane.

(B) Current density ($J$) and power density ($P$) versus potential ($E$) data for a protonic diode sensitized with ~10 mM photoacid. Sequential dark, light, dark (dark-light-dark) data were taken initially (black dots), after 15 min of 405 nm illumination at 1.7 Suns equivalent excitation (magenta dots), and after 25 min in the dark (gray dots), respectively, with the open-circuit photovoltage ($V_{oc}$), short-circuit photocurrent density ($J_{sc}$), bulk area-specific resistance ($ASR_{bulk}^{-1}$), and maximum power point ($P_{max}$) indicated.

(C) Transient open-circuit potential ($E_{oc}$) for a protonic diode with ~10 mM photoacid illuminated through the undyed anion-exchange layer or photoacid-modified cation-exchange layer (purple interval).

(D) $E_{oc}$ and $J_{sc}$ as a function of time, and thus photon fluence rate incident on the anion-exchange-layer side of a protonic diode with ~10 mM photoacid, illuminated for 15 min (purple intervals) and then left in the dark for 25 min (white intervals) for each fluence, and with the condition of 1 Sun equivalent excitation indicated.

(E) Photocurrent action spectrum, reported as an internal quantum yield at $J_{sc}$ (IQY) after 2 min of illumination, and absorptance spectrum of the same protonic diode from (D), and absorptance spectra of protonated and deprotonated structures from (A), as well as a bipolar membrane that does not contain any dyes.

(F) Dark-light-dark Mott-Schottky plots for reverse-bias data that includes best-fits to the Mott-Schottky equation (Equation 2) collected for a protonic diode with ~10 mM photoacid. Electrochemical impedance spectroscopy data over the full range of applied potential biases are shown in Figure S9.

S8), which is a timescale that is longer than that expected for capacitive charging of interfaces and therefore suggests that the materials themselves may be dynamic under illumination. Notably, the magnitude of $V_{oc}$ values is largest after >10 min of continuous illumination (Figures 3C, 3D, and S8), and although there is a small signal consistent with traditional photovoltaic action at early times, this feature is also observed in negative control experiments using little-to-no photoacids (Figure S8) or photoacid-dye-sensitized Nafion only (Figure S7). Negative control experiments meant to result in processes other than excited-state proton transfer, such as heating, excited-state electron transfer, and/or excited-state energy transfer, also resulted in traditional photovoltaic action (Figures S7 and S8). Moreover, $J_{sc}$ values from reverse photovoltaic action are largest 5–15 min into a period of continuous illumination, but then decrease at even longer times (Figures 3D and S7), and are largest when incident photon energy equals

that of electronic transitions in the protonated state of the photoacid (Figure 3E). In addition, observation of a greater-than-unity turnover number (Figure S7) suggests that stoichiometric processes, such as dye or polymer degradation, are not likely the cause of "reverse" photovoltaic action.

Other unique observations, which do not guarantee "reverse" photovoltaic action, are apparent in the Mott-Schottky plot (Figure 3F), where illumination increases $E_{fb}$ even when reported versus dark $E_{oc}$, indicating that $\Phi_{bi}$ increases more than concomitant changes in $|V_{oc}|$. This is consistent with photogeneration of interface dipoles that oppose $\Phi_{bi}$,[7] which can be generated due to differences in mobility of $H^+$ and $OH^-$ and/or trap-state filling, such that additional protonic charge recombination is required to reestablish equilibrium, resulting in a reverse-bias-predicted $E_{fb}$ that is larger than $\Phi_{bi}$. The presence of protonic photoacid trap states is supported by $C_{sc}^{-2}$–$E$ data measured for photoacid-dye-sensitized bipolar-membrane-electrode assemblies (Figure S9). Moreover, the magnitude of the slope of the Mott-Schottky data increases by up to a factor of two under illumination, which, according to Equation 2, implies that the fixed-charge density, $N$, and/or the relative permittivity, $\varepsilon_r$, in the space-charge region decrease to as little as half of their values in the dark. This large of a decrease in $N$ is highly improbable, with details in the supplemental information, and thus this change in slope is more likely due to a decrease in $\varepsilon_r$ in the space-charge region from the effects of photogenerated interface dipoles to align dyes and/or water molecules. Such an effect would result in an *increase* in $\Phi_{bi}$, which is consistent with $E_{fb}$ values measured under illumination.

Collectively, our observations suggest that "reverse" photovoltaic action may be occurring due to slow interface-trap-state filling of protonic photoacid states, changes in polymer morphology,[45,46] alteration of dielectric properties,[47] dynamics of non-protonic mobile charged species,[47] and/or reorganization or transport of water due to changes in its activity, with additional details in the supplemental information. Since our photoacids rarely photogenerate $OH^-$,[42] we also considered that "reverse" photovoltaic action might be due to sharp gradients in the generation profile of $H^+$ only[47–51] across the bipolar-membrane junction, similar to traditional dye-sensitized solar cells, which result in recombination of $H^+$ and $OH^-$ in the anion-exchange layer. However, the tens-of-minutes-long dynamics observed for the growth of "reverse" photovoltaic signals suggest a much more slowly evolving process is responsible for the effect. Irrespective of the underlying mechanism of "reverse" photovoltaic action, it provides unique benefits to traditional photovoltaic action. As predicted by the Shockley diode equation, "reverse" photovoltaic action variations in light intensity have a larger impact on $|V_{oc}|$ and $\Phi_{bi}$ than on $J_{sc}$, which is also limited to values less than $J_o$. This suggests that "reverse" photovoltaic devices may be useful for applications where large voltages are desired—such as water-tolerant implantable ionic gates[52] or low-light optical sensors[53]—and/or where an integrated design precludes use of multiple photocells and power electronics—such as autonomous desalination. Additional work is required to further understand the mechanistic details of "reverse" photovoltaic action in photoacid-dye-sensitized bipolar-membrane-electrode-assembly protonic solar cells.

## EXPERIMENTAL PROCEDURES

### Resource availability

#### *Lead contact*

Further information and requests for resources and materials should be directed to and will be fulfilled by the lead contact, Shane Ardo (ardo@uci.edu).

*Materials availability*

This study did not generate new unique materials.

*Data and code availability*

COMSOL Multiphysics version 5.3 code supporting the current study is available from the lead contact on request.

## Covalent modification of polymers with photoacids

Photoacid dye molecules, 8-hydroxypyrene-1,3,6-trisulfonylethylenediammonium chloride, were synthesized using a previously reported procedure.[40] Subsequently, these photoacid molecules were covalently bonded to poly(perfluorosulfonyl fluoride) Nafion sulfonyl fluoride precursor membranes by submerging precursor membranes in an isopropanol solution containing photoacids, NaOH(aq), and triethylamine to form photoacid-modified Nafion. We followed a previously reported procedure,[37] except that the reaction was carried out at 80 °C rather than 90 °C and the concentration of photoacids in the reaction solution was varied to obtain different extents of membrane functionalization. After this covalent modification and the previously reported work-up procedure, photoacid-modified Nafion was rinsed thoroughly and then stored in 150 mL ultrapure water (Millipore Sigma, Milli-Q Reference Water Purification System) until use.

## Bipolar membrane fabrication

Bipolar membranes were fabricated by first patting photoacid-modified Nafion dry with a Kimwipe and then laying it on a clean glass slide. A piece of Parafilm with a hole in the middle (1.7 cm in diameter) was applied to its surface to expose a controlled upward-facing area of the membrane. The Parafilm|photoacid-modified-Nafion|glass stack was placed on a hotplate (preheated to 80 °C) and allowed to come to temperature at which time the edges of the Parafilm mask were pressed gently to ensure a leakless seal with photoacid-modified Nafion, and then 4 mL of Sustainion XA-9 Alkaline Ionomer (5 wt % in ethanol, Dioxide Materials) was drop cast onto the exposed area, followed by heating for 1 h at 80 °C on the hotplate.

The bipolar membrane fabrication method differed slightly from our prior report[31] in which we laminated photoacid-modified Nafion to a commercial anion-exchange membrane (Neosepta, Astom Corporation) and applied pressure to either side using magnets in the presence of heat, which resulted in occasional gaps at the membrane|membrane interface as well as a gradual increase in ionic resistance over several hours of electrochemical evaluation due to delamination. Since that report, we discovered that depositing the ionomer form of the anion-exchange membrane resulted in a higher quality contact and no noticeable delamination between the cation-exchange layer and anion-exchange layer over days of electrochemical evaluation and months of storage in water.

## Membrane-electrode assembly fabrication

Ion-exchange-membrane-catalyst inks consisted of a mixture of 200 mg of 40% Platinum on HighSurface Area Ketjenblack EC-300J (The Fuel Cell Store) and ionomer. The ionomer used for the cation-exchange-membrane ink was 300 mg of D2021CS Nafion Dispersion (1,100 EW, 20 wt % in alcohol, Ion Power Inc.) and the ionomer used for the anion-exchange-membrane ink was 1.2 g of Sustainion XA-9 Alkaline Ionomer (5 wt % in ethanol). To obtain the ideal viscosity for spray coating, the two formulations were diluted to 5 wt % solids with isopropanol and sonicated for at least 20 min.

Before application of the anion-exchange-membrane-catalyst ink, another Parafilm mask with a hole in the middle (1.2 cm in diameter) was placed over the existing Parafilm|bipolar-membrane|glass stack to ensure that ink would not contact the edges of the bipolar membrane, thus eliminating edge recombination effects and the chance for electrical shunts between the two electrodes during electrochemical evaluation. A circular piece of Parafilm (0.5 cm in diameter) was pressed onto the center of the exposed area of the bipolar membrane to mask the region that would later be illuminated during photoelectrochemical measurements in order to ensure that significant incident light is transmitted to the bipolar-membrane pn-junction. The multi-Parafilm|bipolar-membrane|glass stack (preheated to 80°C) was quickly positioned vertically without continued heating so that the face of the bipolar membrane was oriented perpendicular to the ground. A spray coating gun (Paasche H Series) supplied with an air flow rate of 0.3 L/s was used to deposit ~1 mg Pt/cm$^2$ worth of anion-exchange-membrane-catalyst ink, a roughly 5 μm thick layer, which was then allowed to dry, followed by heating for 10 min at 80°C on the hotplate. Because the same material was used as the bulk anion-exchange layer and the binder in the anion-exchange-membrane-catalyst ink, this procedure resulted in a highly uniform and adherent membrane-electrode-assembly interface. This loading of anion-exchange-membrane-catalyst ink was approximately twice that used for the highest loadings indicated in Figure S1.

The bipolar-membrane stack was then removed from the glass slide and flipped over to expose the photoacid-modified Nafion face. Another set of Parafilm masks (one piece with a 1.2 cm diameter hole in the middle and one 0.5 cm diameter circular piece) was pressed onto the center of the bipolar membrane. The cation-exchange-membrane-catalyst ink was spray coated onto the photoacid-modified Nafion face in the same manner as the anion-exchange-membrane-catalyst ink and then the stack was heated for 10 min at 80°C on the hotplate. Again, this procedure resulted in a highly uniform and adherent membrane-electrode-assembly interface. The Parafilm was removed from the stack to reveal the completed membrane-electrode assembly, which was stored in 200 mL of ultrapure water for >24 h to allow $Cl^-$ counterions in the as-received commercial anion-exchange ionomer, and other unwanted salt ions, to dialyze out of the bipolar membrane, with conductance measured using a conductivity meter (HM Digital, DM-2EC: Dual EC Monitor).

### Membrane-electrode assembly setup

Prior to electrochemical or photoelectrochemical evaluation, each membrane-electrode assembly was patted dry with a Kimwipe and positioned in the center of an acrylic gas flow cell (Fuel Cell Store, FCSU-010B) outfitted with 2 cm × 5 cm carbon-cloth current collectors lightly contacting either side of the membrane-electrode assembly and a 0.5 cm diameter hole in the center to allow significant incident light to be transmitted to the bipolar-membrane pn-junction during photoelectrochemical evaluation. Forming gas (5 mol % $H_2$, 95 mol % $N_2$) flowed at a rate of 1 mL/s through two fritted bubblers to achieve 100% relative humidity, and then through a T-splitter that was connected to each chamber of the acrylic test cell using a silicone tube (2 mm inner diameter). After flowing across each face of the membrane-electrode assembly, gas exited the cell via silicone tubes (2 mm inner diameter) located at the top of each chamber of the acrylic cell. Each membrane-electrode assembly was preconditioned in humidified forming gas for 1 h prior to collection of data using a potentiostat (Biologic, SP-300). This served to drive off residual unwanted soluble carbonate species and ensure a stable initial open-circuit potential that was measured to be <5 mV in magnitude. Ideally, this assembly and use of two reversible hydrogen electrodes should result in an open-circuit potential equal to zero, due to having no difference in the electrochemical potential of $H^+$

across the cell and no difference in the electrochemical potential of $OH^-$ across the cell, with details in the supplemental information.

### Steady-state (photo)electrochemistry

Current versus potential data were obtained both in the dark and in the light by performing chronoamperometry measurements for a series of applied potential biases. For data obtained under illumination, and for accompanying data obtained for the same sample in the dark, current values were converted into current densities using 0.20 $cm^2$, the area of the membrane-electrode assembly that was not covered by Pt/C catalyst or the carbon-cloth current collector. For samples that were only evaluated in the dark, current values were converted into current densities using 1.0 $cm^2$, the area of the membrane-electrode assembly that was covered by Pt/C catalyst. For measurements performed in the dark, the current was recorded 15 s after application of the potential bias to ensure the system had reached a quasi-steady-state condition. The illumination source for all measurements, besides spectral response, was a 405 nm laser diode (Thorlabs, L405G1) that was driven at 1 A and held at 22°C (Thorlabs, ITC4001) in a temperature-controlled mount (Thorlabs, LDM90). The total power output of the laser diode was 175 mW as measured by a thermopile (Thorlabs, S310C and PM100D), and the beam spot slightly overfilled the 0.20 $cm^2$ center area of the membrane-electrode assembly that was not covered by Pt/C catalyst or the carbon-cloth current collector, such that ~15 mW (~75 mW/$cm^2$) passed through the front face of the acrylic gas flow cell and reached the membrane. Open-circuit photovoltage data were obtained by performing an open-circuit potential measurement in the dark and then under 15 min of illumination, over which time it reached a quasi-steady-state condition. Illumination was then ceased to allow for re-equilibration in the dark for 25 min before the "dark again" datasets were collected. A similar procedure was used to collect the electrochemical impedance spectroscopy data shown in Figure 3F. Each set of current versus potential data was plotted on a common x axis by referencing to the open-circuit potential measured before the initial "dark" dataset was collected.

Direct applied potential biases were corrected for contributions due to ohmic resistance by subtracting $J \times ASR_{bulk}$, unless $J \times ASR_{bulk}$ was calculated to be smaller than the experimental noise. For example, no correction was made to the data shown in Figure 3B, because $J \times ASR_{bulk}$ was <3 μV over the potential range displayed. Light-to-electrical power conversion efficiencies were calculated from current versus potential data by dividing the maximum output electrical power density by the input photon irradiance. To simulate sunlight conditions, the input photon irradiance was set equal to the number of Suns equivalent excitation times the 1 Sun irradiance of 100 mW/$cm^2$.

Spectral response measurements used to generate the photocurrent action spectrum (Figure 3E) were collected under short-circuit conditions by applying the dark open-circuit potential, followed by underfilled illumination of the membrane-electrode assembly using laser pointers in the following order and with the following excitation wavelengths (in nm): 405, 450, 520, 532, 635, and 650 (Thorlabs, CPS series driven by LDS5), and, respectively, with the following output powers (in mW): 4.34, 4.15, 4.55, 5.38, 4.47, and 4.33, as measured by a microscope power sensor head (Thorlabs, S170C). Short-circuit current densities were recorded for a given wavelength after 2 min of illumination, and then the assembly was allowed to re-equilibrate in the dark for 4 min before initiating excitation using the next illumination wavelength in the series. External quantum yields were determined by dividing short-circuit current densities by the product of the Faraday constant and the incident photon fluence rate. Internal quantum yields were determined by dividing these external quantum yields by the absorptance at each excitation wavelength.

Incident photon fluence rate was determined by multiplying the measured output power by the transmittance of the illuminated side of the acrylic gas flow cell; for example, only ~59% of incident photons at 405 nm transmitted through the acrylic.

Datasets for $V_{oc}$ and datasets for $J_{sc}$ each as a function of photon fluence rate were measured using the 405 nm laser diode driven at 1 A with light passing through neutral density filters of optical densities of 1, 0.6, 0.4, 0.2, and 0.1 (Thorlabs), in that order, and mounted in a motorized filter wheel (Thorlabs, FW102C) before reaching the membrane-electrode assembly. Data were recorded in the presence of a given neutral density filter after 15 min of illumination, and then the assembly was allowed to re-equilibrate in the dark for 25 min before initiating excitation through the next neutral density filter in the series.

### (Photo)electrochemical impedance spectroscopy

Electrochemical impedance spectroscopy data were obtained by applying a DC bias to a membrane-electrode assembly for 15 s and then triggering a sinusoidal AC perturbation ($\pm$10 mV) at frequencies ranging from 100 kHz to 10 Hz, in that order. The resultant data were fit to the simple Randles circuit without contributions due to mass transport, consisting of a resistor ($R_{bulk}$) in series with a nonideal parallel $R_{sc}C_{sc}$ circuit element. A more complex circuit would have resulted in better fits to the data, especially at large forward biases of >0.5 V, but we decided that a simple representation was preferred over capturing all minor features in the data. When fitting, $R_{bulk}$ was held at a constant value determined via linear extrapolation of the high frequency to the x-intercept of the Nyquist plot, and all other parameters were allowed to float. Raw data were weighted by a value of one for best-fit data shown in Figures 2B, 2C, and 3F, and, for comparison, by the magnitude of the impedance for best-fit data shown in Figure S4. At large forward biases of >0.5 V and at low frequencies, a feature consistent with mass-transport-limited behavior was observed. We did not include those points during best-fitting (see Nyquist and Bode plots in Figure S4 where datapoints do not have a corresponding overlapping best-fit line), because those data were likely in part limited by the delivery of $H_2$ to the reversible hydrogen electrodes and thus not representative of behavior due to the bipolar membrane.

A nonideal capacitor is required to model charging of the pn-junction space-charge region. This is reasonably ascribed to inhomogeneity in the space-charge region that results in a distribution of capacitances and can be represented by a constant phase element ($Q_{sc}$), as others have previously observed for bipolar membranes.[29,54] The potential-dependent capacitance of the space-charge region, $C_{sc}$ (F/cm$^2$), is calculated as follows:

$$C_{sc} = \frac{(Q_{sc} \times R_{sc})^{(1/a_{sc})}}{R_{sc} \times A} \qquad \text{(Equation 3)}$$

where $Q_{sc}$ is the admittance at a frequency of 1 rad/s ($\Omega^{-1}$ $s^{a_{sc}}$), $R_{sc}$ is the resistance for transport of charges across the space-charge region ($\Omega$), $A$ is the area of the membrane-electrode assembly that was covered by Pt/C catalyst (cm$^2$), and $a_{sc}$ is the capacitive ideality factor; values for $a_{sc}$ lie in the range (0, 1), with $a_{sc}$ = 1 indicating a perfectly homogenous capacitive interface, such that $C_{sc} = Q_{sc}/A$, and $a_{sc}$ = 0 representing a completely inhomogeneous interface with infinite capacitance.

Mott-Schottky plots of the reverse bias data were extrapolated to determine the flat-band potential, $E_{fb}$, and exchange current density at both ($E_{oc}$, $J_o$) and ($E_{fb}$, $J_o'$). Extrapolation of the forward bias data were less reliable to approximate $J_o$ because of its multiexponential behavior and the few number of datapoints available under the condition

of a low forward bias. The density of fixed-charge groups in the anion-exchange layer is consistent with a smaller number of electroactive dopants than in Nafion. This point is supported by the observation that $ASR_{bulk}$ of an anion-exchange-membrane-electrode assembly is on the order of 100 $\Omega$-cm$^2$, whereas that of a cation-exchange-membrane-electrode assembly is on the order of 10 $\Omega$-cm$^2$ (Figure S2), also suggesting that $ASR_{bulk}$ of the bipolar membrane is dominated by the anion-exchange layer.

### Data analysis

When indicated, data are reported as the mean $\pm$ standard deviation. Linear least-squares best-fit analyses used the Levenberg-Marquardt algorithm and non-linear least-squares best-fit analyses of the electrochemical impedance spectroscopy data used the Randomize + Simplex method.

## SUPPLEMENTAL INFORMATION

Supplemental information can be found online at https://doi.org/10.1016/j.joule.2021.06.016.

## ACKNOWLEDGMENTS

The authors are grateful for financial support from the Gordon and Betty Moore Foundation under a Moore Inventor Fellowship (GBMF grant #5641), Research Corporation for Science Advancement under a Cottrell Scholar Award (award #24169), Nissan Chemical Corporation for sponsored research support, and the U.S. Department of Energy Office of Science under an Early Career Research Program Award (DE-SC0019162). SEM and EDS measurements were performed using instrumentation funded in part by the National Science Foundation Center for Chemistry at the Space-Time Limit (CHE-0802913). We also acknowledge the UCI Chemical, Applied and Materials Physics (ChAMP) Program for COMSOL Multiphysics instruction and support. We also thank Adam Nielander, CX Xiang, Alec Talin, Shannon Boettcher, Jason Cooper, Matt Sheldon, and Shu Hu for helpful and thought-provoking conversations related to this work.

## AUTHOR CONTRIBUTIONS

L.S. contributed to the design of experiments, prepared all samples, and performed all measurements, including subsequent analysis and interpretation of all data reported in this manuscript, and contributed to the preparation of the manuscript. W.W. and L.A.R. contributed to the design of the initial experiments, prepared the initial samples, and performed the initial electrochemical measurements, including subsequent data analysis and interpretation. S.A. proposed the research and contributed to experimental design, data interpretation, and preparation of the manuscript.

## DECLARATION OF INTERESTS

Co-authors are co-inventors of the following pending patent applications that are relevant to this article: US20180065095 and WO2018049061 (S.A. and W.W.), US20190217255 and WO2019191326 (S.A., W.W., L.A.R., and L.S.). S.A. received sponsored research funding support by Nissan Chemical Corporation for work related to that reported in this article. W.W. is currently working at Intel and L.A.R. is currently working at Intelligent Optical Systems.

Received: April 22, 2021
Revised: June 11, 2021
Accepted: June 16, 2021
Published: July 20, 2021

## REFERENCES


1. Shockley, W. (1949). The theory of *p-n* junctions in semiconductors and *p-n* junction transistors. Bell Syst. Tech. J. *28*, 435–489.
2. Hussey, L.W. (1953). Semiconductor diode gates. Bell Syst. Tech. J. *32*, 1137–1154.
3. Chapin, D.M., Fuller, C.S., and Pearson, G.L. (1954). A new silicon p-n junction photocell for converting solar radiation into electrical power. J. Appl. Phys. *25*, 676–677.
4. Pierret, R.F. (1996). Semiconductor Device Fundamentals, Sixth Edition (Addison-Wesley).
5. Sze, S.M., and Ng, K.K. (2006). Physics of Semiconductor Devices (John Wiley & Sons).
6. Würfel, P. (2005). Physics of Solar Cells (Wiley).
7. Fonash, S.J. (2010). Solar Cell Device Physics (Academic Press/Elsevier).
8. Bockris, J.O.'M., and Reddy, A.K.N. (1973). Modern Electrochemistry (Springer).
9. Bard, A.J., and Faulker, L.R. (2001). Electrochemical Methods: Fundamentals and Applications, Second Edition (Wiley).
10. Guan, W., Fan, R., and Reed, M.A. (2011). Field-effect reconfigurable nanofluidic ionic diodes. Nat. Commun. *2*, 506.
11. Van De Burgt, Y., Lubberman, E., Fuller, E.J., Keene, S.T., Faria, G.C., Agarwal, S., Marinella, M.J., Alec Talin, A., and Salleo, A. (2017). A non-volatile organic electrochemical device as a low-voltage artificial synapse for neuromorphic computing. Nat. Mater. *16*, 414–418.
12. Kong, J., Franklin, N.R., Zhou, C., Chapline, M.G., Peng, S., Cho, K., and Dai, H. (2000). Nanotube molecular wires as chemical sensors. Science *287*, 622–625.
13. Wang, Q., Hisatomi, T., Jia, Q., Tokudome, H., Zhong, M., Wang, C., Pan, Z., Takata, T., Nakabayashi, M., Shibata, N., et al. (2016). Scalable water splitting on particulate photocatalyst sheets with a solar-to-hydrogen energy conversion efficiency exceeding 1%. Nat. Mater. *15*, 611–615.
14. Tembhurne, S., Nandjou, F., and Haussener, S. (2019). A thermally synergistic photo-electrochemical hydrogen generator operating under concentrated solar irradiation. Nat. Energy *4*, 399–407.
15. Fuller, C.S. (1956). Some analogies between semiconductors and electrolyte solutions. Record of Chem. Prog. *17*, 75–93.
16. Lovreček, B., Despić, A., and Bockris, J.O.'M. (1959). Electrolytic junctions with rectifying properties. J. Phys. Chem. *63*, 750–751.
17. Eigen, M., and De Maeyer, L. (1958). Self-dissociation and protonic charge transport in water and ice. Proc. R. Soc. Lond. A *247*, 505–533.
18. Shimizu, K., Yoshida, Y., Senō, M., and Nozaki, H. (1968). The rectification effects using the ices doped with electrolytes. Bull. Chem. Soc. Jpn. *41*, 2325–2330.
19. Langer, J.J. (1985). A protonic rectifier diode. Appl. Phys. A *38*, 59–60.
20. Petrenko, V.F., and Maeno, N. (1987). Ice field transistor. J. Phys. Colloques. *48*, 1–115.
21. Petrenko, V.F. (1993). Electrical Properties of Ice (U.S. Army Corps of Engineers, Cold Regions Research & Engineering Laboratory).
22. Maslov, V.N., and Zotov, Y.A. (1968). Water as a semiconductor. Russ. Chem. Rev. *37*, 310–315.
23. Tolbert, L.M., and Solntsev, K.M. (2002). Excited-state proton transfer: From constrained systems to "super" photoacids to superfast proton transfer. Acc. Chem. Res. *35*, 19–27.
24. Simons, R., and Khanarian, G. (1978). Water dissociation in bipolar membranes: experiments and theory. J. Membrain. Biol. *38*, 11–30.
25. Simons, R. (1979). Strong electric field effects on proton transfer between membrane-bound amines and water. Nature *280*, 824–826.
26. Ramírez, P., Rapp, H.J., Reichle, S., Strathmann, H., and Mafé, S. (1992). Current-voltage curves of bipolar membranes. J. Appl. Phys. *72*, 259–264.
27. Mafé, S., Ramírez, P., and Alcaraz, A. (1998). Electric field-assisted proton transfer and water dissociation at the junction of a fixed-charge bipolar membrane. Chem. Phys. Lett. *294*, 406–412.
28. Craig, N.P. (2013). Electrochemical behavior of bipolar membranes., PhD thesis (University of California Berkeley).
29. Yan, Z., Zhu, L., Li, Y.C., Wycisk, R.J., Pintauro, P.N., Hickner, M.A., and Mallouk, T.E. (2018). The balance of electric field and interfacial catalysis in promoting water dissociation in bipolar membranes. Energy Environ. Sci. *11*, 2235–2245.
30. Grew, K.N., McClure, J.P., Chu, D., Kohl, P.A., and Ahlfield, J.M. (2016). Understanding transport at the acid-alkaline interface of bipolar membranes. J. Electrochem. Soc. *163*, F1572–F1587.
31. White, W., Sanborn, C.D., Fabian, D.M., and Ardo, S. (2018). Conversion of visible light into ionic power using photoacid-dye-sensitized bipolar ion-exchange membranes. Joule *2*, 94–109.
32. Lu, Z., Polizos, G., Macdonald, D.D., and Manias, E. (2008). State of water in perfluorosulfonic ionomer (Nafion 117) proton exchange membranes. J. Electrochem. Soc. *155*, B163–B171.
33. Liu, Z., Yang, H., Kutz, R., and Masel, R.I. (2018). $CO_2$ electrolysis to CO and $O_2$ at high selectivity, stability and efficiency using Sustainion membranes. J. Electrochem. Soc. *165*, J3371–J3377.
34. Kusoglu, A., and Weber, A.Z. (2017). New insights into perfluorinated sulfonic-acid ionomers. Chem. Rev. *117*, 987–1104.
35. Talin, A.A., Léonard, F., Swartzentruber, B.S., Wang, X., and Hersee, S.D. (2008). Unusually strong space-charge-limited current in thin wires. Phys. Rev. Lett. *101*, 076802.
36. Röhr, J.A., Moia, D., Haque, S.A., Kirchartz, T., and Nelson, J. (2018). Exploring the validity and limitations of the Mott-Gurney law for charge-carrier mobility determination of semiconducting thin-films. J. Phys. Condens. Matter *30*, 105901.
37. White, W., Sanborn, C.D., Reiter, R.S., Fabian, D.M., and Ardo, S. (2017). Observation of photovoltaic action from photoacid-modified Nafion due to light-driven ion transport. J. Am. Chem. Soc. *139*, 11726–11733.
38. White, W., Luo, S., Bhide, R., Sanborn, C.D., Baranov, M.S., Solntsev, K.M., and Ardo, S. (2019). Evaluation of the role that photoacid excited-state acidity has on photovoltage and photocurrent of dye-sensitized ion-exchange membranes. Proceedings of the SPIE Phys. Chem. Semicond. Mater. Interfaces *XVIII*, 110840E, 11084.
39. Reiter, R.S., White, W., and Ardo, S. (2016). Electrochemical characterization of commercial bipolar membranes under electrolyte conditions relevant to solar fuels technologies. J. Electrochem. Soc. *163*, H3132–H3134.
40. Sanborn, C.D., Chacko, J.V., Digman, M., and Ardo, S. (2019). Interfacial and nanoconfinement effects decrease the excited-state acidity of polymer-bound photoacids. Chem *5*, 1648–1670.
41. Chen, H.Y., and Ardo, S. (2018). Direct observation of sequential oxidations of a titania-bound molecular proxy catalyst generated through illumination of molecular sensitizers. Nat. Chem. *10*, 17–23.
42. Luo, S., White, W., Cardon, J.M., and Ardo, S. (2021). Clarification of Mechanisms of Protonic Photovoltaic Action Initiated by Photoexcitation of Strong Photoacids Covalently Bound to Hydrated Nafion Cation-Exchange Membranes Wetted by Aqueous Electrolytes. Energy & Environmental Science. https://doi.org/10.1039/D1EE00482D.
43. Strandberg, R. (2015). Theoretical efficiency limits for thermoradiative energy conversion. J. Appl. Phys. *117*, 055105.
44. Deppe, T., and Munday, J.N. (2020). Nighttime photovoltaic cells: electrical power generation by optically coupling with deep space. ACS Photonics *7*, 1–9.
45. Su, G.M., White, W., Renna, L.A., Feng, J., Ardo, S., and Wang, C. (2019). Photoacid-modified Nafion membrane morphology determined by resonant X-ray scattering and spectroscopy. ACS Macro Lett *8*, 1353–1359.
46. Grew, K.N., and Chiu, W.K.S. (2020). Stability & kinetics of the bipolar membrane interface: implications for electrochemical technologies. J. Electrochem. Soc. *167*, 164513.

47. Moerner, W.E. (2001). Photorefractive polymers. In Encyclopedia of materials: Science and Technology (Elsevier), pp. 6961–6968.

48. Pockett, A., Raptis, D., Meroni, S.M.P., Baker, J., Watson, T., and Carnie, M. (2019). Origin of exceptionally slow light soaking effect in mesoporous carbon perovskite solar cells with AVA additive. J. Phys. Chem. C *123*, 11414–11421.

49. Green, M.A. (1976). The depletion layer collection efficiency for p-n junction, Schottky diode, and surface insulator solar cells. J. Appl. Phys. *47*, 547–554.

50. Reichman, J. (1981). Collection efficiency of low-mobility solar cells. Appl. Phys. Lett. *38*, 251–253.

51. Kumar, A., and Lewis, N.S. (1990). Short-wavelength spectral response properties of semiconductor/liquid junctions. J. Phys. Chem. *94*, 6002–6009.

52. Tybrandt, K., Forchheimer, R., and Berggren, M. (2012). Logic gates based on ion transistors. Nat. Commun. *3*, 871.

53. Kim, H., Jung, Y., Doh, I.J., Lozano-Mahecha, R.A., Applegate, B., and Bae, E. (2017). Smartphone-based low light detection for bioluminescence application. Sci. Rep. *7*, 40203.

54. Blommaert, M.A., Vermaas, D.A., Izelaar, B., In't Veen, B., and Smith, W.A. (2019). Electrochemical impedance spectroscopy as a performance indicator of water dissociation in bipolar membranes. J. Mater. Chem. A *7*, 19060–19069.

Joule

CellPress

Article

# Turning water into a protonic diode and solar cell via doping and dye sensitization

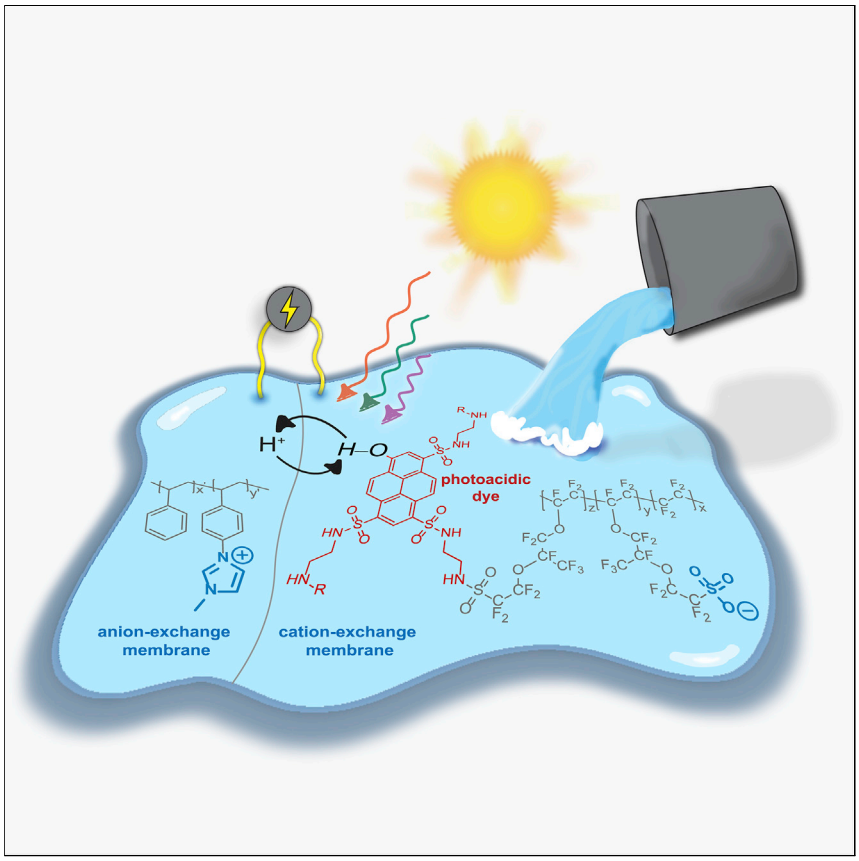


Bipolar ion-exchange membranes serve as scaffolds for dopants that, when infiltrated with water, release protons and hydroxides as mobile-charge-carrier species and exhibit protonic diode behavior. Sensitization of current-rectifying bipolar membranes to visible light through covalent modification with photoacid dye molecules resulted in the observation of "reverse" photovoltaic action. These diode and photovoltaic protonic functions motivate further study of ionic analogs to electronic devices, which may be important for applications where electronics interface directly with aqueous solutions.

Leanna Schulte, William White, Lawrence A. Renna, Shane Ardo

ardo@uci.edu

## Highlights

Demonstration of high-quality bipolar-membrane-electrode-assembly protonic diodes

Space-charge depletion region width is dictated by anion-exchange-layer properties

Quasi-electrochemical potentials for $H^+$ and $OH^-$ are out-of-equilibrium over ~30 nm

Observation of "reverse" photovoltaic action likely due to dynamic polymer processes

Schulte et al., Joule 5, 2380–2394
September 15, 2021 
https://doi.org/10.1016/j.joule.2021.06.016